

## Equilibrium shape of nano-cavities in H implanted ZnO

K. S. Chan, L. Vines, L. Li, C. Jagadish, B. G. Svensson, and J. Wong-Leung

Citation: [Applied Physics Letters](#) **106**, 212102 (2015); doi: 10.1063/1.4921788

View online: <http://dx.doi.org/10.1063/1.4921788>

View Table of Contents: <http://scitation.aip.org/content/aip/journal/apl/106/21?ver=pdfcov>

Published by the [AIP Publishing](#)

---

### Articles you may be interested in

[Mn doped nanostructure ZnO thin film for photo sensor and gas sensor application](#)

AIP Conf. Proc. **1512**, 652 (2013); 10.1063/1.4791206

[ZnO nano flowers formation by microwave assisted chemical bath deposition technique](#)

AIP Conf. Proc. **1451**, 157 (2012); 10.1063/1.4732399

[Photoluminescence quenching processes by NO<sub>2</sub> adsorption in ZnO nanostructured films](#)

J. Appl. Phys. **111**, 073520 (2012); 10.1063/1.3700251

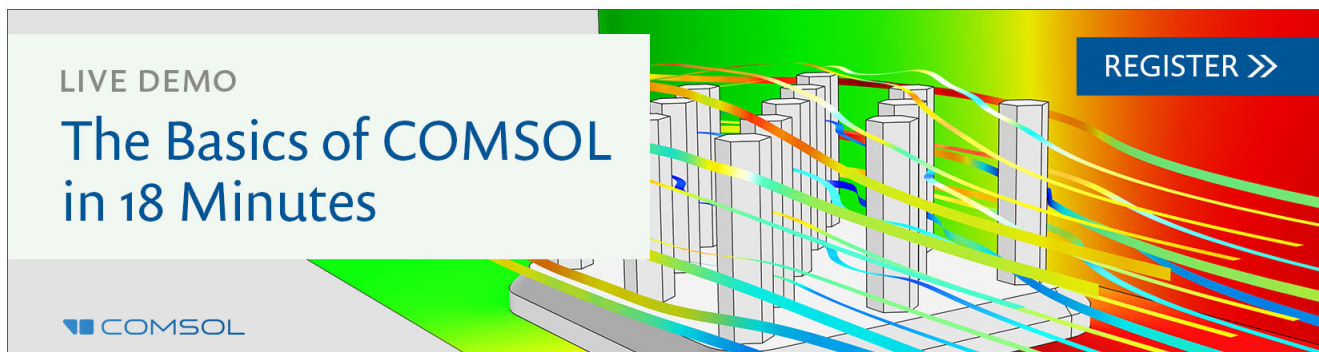
[Zinc and oxygen vacancies in ZnO nanorods](#)

J. Appl. Phys. **106**, 104307 (2009); 10.1063/1.3259413

[Tunable growth of ZnO nanorods synthesized in aqueous solutions at low temperatures](#)

J. Vac. Sci. Technol. B **24**, 288 (2006); 10.1116/1.2163889

---

A promotional banner for COMSOL software. It features a 3D bar chart with colorful lines representing data trends. The text 'LIVE DEMO' is in the top left, 'The Basics of COMSOL in 18 Minutes' is in the center, and 'REGISTER >>' is in a blue button on the right. The COMSOL logo is in the bottom left.

LIVE DEMO

# The Basics of COMSOL in 18 Minutes

REGISTER >>

COMSOL

## Equilibrium shape of nano-cavities in H implanted ZnO

K. S. Chan,<sup>1,a)</sup> L. Vines,<sup>2</sup> L. Li,<sup>3</sup> C. Jagadish,<sup>1</sup> B. G. Svensson,<sup>2</sup> and J. Wong-Leung<sup>1,4,b)</sup>

<sup>1</sup>Department of Electronic Materials Engineering, Research School of Physics and Engineering, The Australian National University, Canberra, Australian Capital Territory 2601, Australia

<sup>2</sup>Department of Physics/Centre for Materials Science and Nanotechnology, University of Oslo, P.O. Box 1048 Blindern, N-0316 Oslo, Norway

<sup>3</sup>Australian National Fabrication Facility ACT Node, Research School of Physics and Engineering, The Australian National University, Canberra, Australian Capital Territory 2601, Australia

<sup>4</sup>Centre for Advanced Microscopy, The Australian National University, Canberra, Australian Capital Territory 2601, Australia

(Received 12 March 2015; accepted 17 May 2015; published online 26 May 2015)

Thermally equilibrated nano-cavities are formed in ZnO by H implantation and subsequent high temperature annealing to determine the relative surface formation energies and step energies of ZnO from reverse Wulff construction and related analysis. H adsorption, vicinal surfaces, and surface polarity are found to play an important role in determining the final thermal equilibrium shape of the nano-cavities. Under H coverage, the O-terminated surface shows a significantly lower surface formation energy than the Zn-terminated surface. © 2015 AIP Publishing LLC.

[<http://dx.doi.org/10.1063/1.4921788>]

A good understanding of surface properties is crucial to determine and control the anisotropic growth of semiconductor bulk, thin films, and nanostructures. Theoretically, the surface formation energies of a crystal can be obtained from 1st principles density functional theory (DFT) calculations. This has been studied extensively for ZnO,<sup>1–6</sup> a direct wide bandgap semiconductor that is promising for the next generation optoelectronic devices, transparent electronics, and solar cells. However, it can be challenging to determine the surface formation energies from 1st principles methods, especially for ZnO. For instance, DFT calculations assume that ZnO polar surfaces are stabilized via a negative charge transfer from O to Zn terminated surface,<sup>7</sup> but such a mechanism has so far not been observed experimentally.<sup>8</sup> It has also been shown that charge transfer may not be the only stabilization mechanism as it cannot completely neutralize the internal electric field created by the diverging electrostatic energy at the ZnO polar surfaces.<sup>2</sup> In practice, impurities adsorption and surface/subsurface defects can also cause chemical interaction and alter the formation energy and stability of the surfaces. In particular, theory predicts that surface energy of the O-terminated surface can change significantly with different H coverage, H chemical potential, and temperature.<sup>9,10</sup>

Experimentally, the relative surface energies can be determined if there is sufficient surface diffusion for equilibrium shape to form.<sup>11</sup> Equilibrium shape occurs as a result of the minimization of total surface energy with the constraint of a constant volume, which can be difficult to achieve in macroscopic crystals.<sup>11</sup> Nano-voids found in various implanted semiconductors<sup>11–15</sup> can achieve thermal equilibrium shape more easily. The facets of these thermally equilibrated cavities have been used to determine the surface formation energy in Si.<sup>11,13</sup> However, for ZnO,

reports of ion induced nanostructuring are still scarce due to an outstandingly high rate of dynamic defect annealing during implantation.<sup>16</sup> This may explain why there is still no experimental study on surface energy of ZnO using ion-induced nano-cavities.

In the present work, we will extend the approach used by Eaglesham *et al.*<sup>13</sup> and Follstaedt<sup>11</sup> for Si to determine the formation energies of polar, non-polar, and several low-index semi-polar surfaces in ZnO. Equilibrium shape is obtained by forming nano-voids via H implantation followed by high temperature annealing. From secondary ion mass spectrometry analysis (not shown), a small amount of implanted H (with peak concentration  $\sim 5 \times 10^{18} \text{ cm}^{-3}$  or 0.12 at. %) is still present in the void region even after annealing at 950 °C. Consequently, it is reasonable to assume that equilibrium shape of the voids and hence the surface energies extracted here apply to a H-rich environment. As H is present in almost all the ZnO growth and processing environment, it is pertinent to investigate the formation energies of H-chemisorbed surfaces in ZnO.

100 keV H<sup>-</sup> ions were implanted into (0001) Zn polar surface of hydrothermally grown single crystal ZnO to a dose of  $1 \times 10^{17} \text{ cm}^{-2}$  at room temperature using a NEC 5SDH-4 tandem accelerator with maximum terminal voltage of 1.7 MV. A 10° beam tilt angle was used to minimize channeling.<sup>17</sup> The samples were then annealed in air for 1 h for void formation at the projected range of implantation  $R_p$ .<sup>18</sup> The voids were analyzed by cross section transmission electron microscopy (XTEM) and plan view transmission electron microscopy (PVTEM) using a Philips CM300 instrument operated at 300 kV (LaB<sub>6</sub> filament) or a JEOL 2100F instrument operated at 200 kV (field emission gun). A through focal series was performed to identify the voids using the reversal of contrast of Fresnel fringes at different foci condition.<sup>19</sup> Shape of the nano-cavities was identified by imaging the XTEM samples along m- and a-axis and the PVTEM samples along c-axis. XTEM samples were

<sup>a)</sup>Electronic mail: keng.chan@anu.edu.au

<sup>b)</sup>Electronic mail: jenny.wongleung@anu.edu.au

prepared by mechanical polishing with a tripod polisher, followed by further thinning to electron transparency by Ar beam using a Gatan Model 691 Precision Ion Polishing System for  $\sim 1$  h at  $-168$  °C. PVTEM samples were prepared by focused ion beam (FIB) using a Ga beam in a FEI Helios 600 nanoLAB system.

Upon annealing at  $800$  °C, TEM analysis shows the formation of well faceted voids at  $R_p$ . Annealing at higher temperature at  $950$  °C did not change the voids' shape, while samples annealed at lower temperatures show voids that are more rounded and irregular in shape.<sup>18,20</sup> As a result, the criterion for equilibrium shape as established in Eaglesham *et al.*<sup>13,21</sup> is satisfied after heat treatment at  $800$  °C for 1 h: small, faceted nano-voids identical in shape irrespective of size, are observed at  $R_p$  (also see Ref. 18). The equilibrium shape of these H implantation-induced cavities is also consistent with those found in porous ZnO nanowires.<sup>22</sup>

Figs. 1(a) and 1(c) show the XTEM images of typical nano-cavities, and corresponding schematic diagrams outlining the planar orientations of the different facets, along (a) and (b)  $[1\bar{1}00]$  and (c) and (d)  $[1\bar{2}10]$ , respectively. These nano-cavities, which are found in H implanted samples after  $800$  °C, show long facets along non-polar  $\{10\bar{1}0\}$  and  $\{11\bar{2}0\}$  surfaces, and semi-polar surfaces. Additionally, short truncated-like internal polar surfaces are also found in some larger voids, with more prominent  $(000\bar{1})$  O-terminated facets compared to Zn ones. Interestingly, the semi-polar facets display a polarity difference, where higher indices are observed for those adjacent to the  $(0001)$  Zn-terminated polar facet compared to the  $(000\bar{1})$  O-terminated ones. The former semi-polar facets will be hereafter referred to as *Zn semi-polar planes* ( $hkil$  where  $l > 0$ ) and the latter as *O semi-polar planes* ( $hkil$  where  $l < 0$ ). Statistical analysis on the semi-polar facets

was performed on 40 voids imaged along each zone axis. For voids imaged along  $[1\bar{1}00]$  zone axis, for O semi-polar facets, 53% are  $\{11\bar{2}4\}$ , 41% are  $\{11\bar{2}5\}$ , and 6% are  $\{11\bar{2}6\}$ ; for Zn semi-polar facets, 28% are  $\{11\bar{2}6\}$ , 40% are  $\{11\bar{2}7\}$ , and 32% are  $\{11\bar{2}8\}$ . On the other hand, for voids imaged along  $[1\bar{2}10]$  zone axis, for O semi-polar facets, 19% are  $\{10\bar{1}2\}$ , 81% are  $\{10\bar{1}3\}$ ; for Zn semi-polar facets, 26% are  $\{10\bar{1}3\}$ , 61% are  $\{10\bar{1}4\}$ , 13% are  $\{10\bar{1}5\}$ . The voids selected for Wulff construction have the most frequently observed semi-polar facets, as demonstrated in the line diagram (Wulff shape) in Figs. 1(b) and 1(d). Furthermore, these voids are large enough for the O internal surface/facets to be observable, so formation energy of the O-terminated surface can be extracted. To obtain 3-dimensional information of the voids, a plan view section of the sample was prepared by FIB so that a thin layer at  $R_p$  was imaged. Fig. 1(e) shows a typical PVTEM image of voids viewed along c-axis. From Fig. 1(f), the voids show clear faceting on alternate non-polar  $\{10\bar{1}0\}$  and (shorter)  $\{11\bar{2}0\}$  facets.

Wulff construction states that the equilibrium shape of a crystal has an interior point (Wulff point) where the perpendicular distance,  $r_i$  from its exterior face to the interior point is proportional to the surface formation energy of the face,  $\gamma$ .<sup>23,24</sup> Wulff point is the center of mass of the Wulff shapes in Figs. 1(b), 1(d), and 1(f).<sup>13</sup> We note here that a complete  $\gamma$  plot can only be constructed for an equilibrium shape with rounded corners.<sup>21</sup> However, for those in Figs. 1(b), 1(d), and 1(f) that have sharp corners, only a portion of the complete  $\gamma$  plot can be constructed.<sup>21</sup> By using the fact that  $\gamma(\theta)/r_i(\theta) = \text{constant}$ ,  $r_i(\theta)$  is measured from the Wulff point with  $\theta$  spacing of  $2^\circ$  for each Wulff shapes to obtain the corresponding  $\gamma(\theta)$ . The resulting  $\gamma(\theta)$  vs  $\theta$  plot that is averaged over 3 voids for each zone axis is shown in Fig. 2. For clarity, these  $\gamma(\theta)$  vs  $\theta$  plots

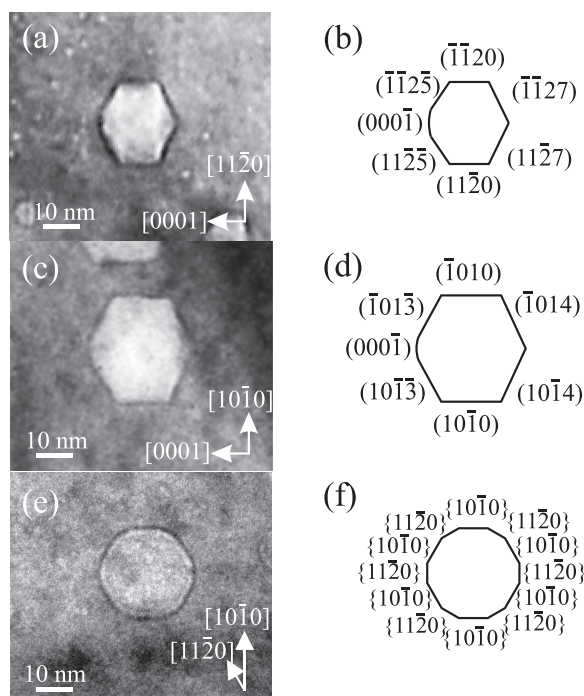


FIG. 1. TEM images of typical thermally equilibrated nano-cavities along (a)  $[1\bar{1}00]$ , (c)  $[1\bar{2}10]$ , and (e)  $[0001]$  zone axes, with the corresponding schematics of their planar facets outlined in (b), (d), and (f), respectively.

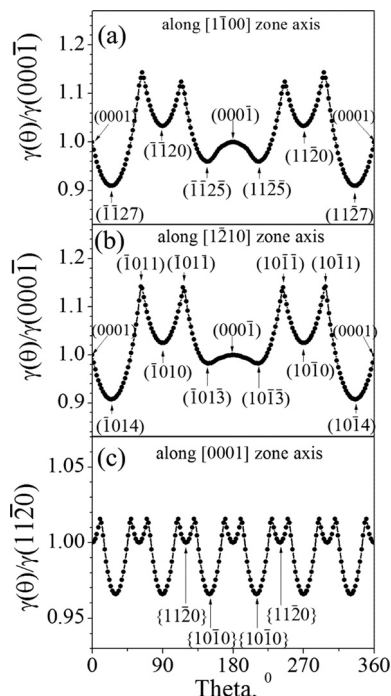


FIG. 2. Surface formation energy  $\gamma(\theta)$  vs  $\theta$  plots extracted from reverse Wulff construction and averaged over 3 voids each along (a)  $[1\bar{1}00]$ , (b)  $[1\bar{2}10]$ , and (c)  $[0001]$  zone axes.

are symmetrized by assuming that the internal surfaces are mirrored around c-axis for XTEM images and m-axis for PVTEM images. For each  $\gamma(\theta)$  plot in Figs. 2(a) and 2(b), there are 6 minima, each representing the surface formation energy  $\gamma$  of a particular facet in the equilibrium shape. The global minima are  $\{11\bar{2}7\}$  and  $\{10\bar{1}4\}$  in their respective zone axes. The facets with the second lowest  $\gamma$  values in their respective zone axes in Figs. 2(a) and 2(b) are  $\{11\bar{2}5\}$  and  $\{10\bar{1}3\}$ . Here,  $\gamma(\{11\bar{2}5\}) \approx 1.06 \gamma(\{11\bar{2}7\})$  and  $\gamma(\{10\bar{1}3\}) \approx 1.08 \gamma(\{10\bar{1}4\})$ . The minima with the highest  $\gamma$  values are the non-polar planes, where  $\{11\bar{2}0\}$  and  $\{10\bar{1}0\}$  have ratios of 1.03 and 1.02, respectively, when compared to  $\gamma(000\bar{1})$ . In addition, the surfaces  $(0001)$ ,  $(000\bar{1})$ , and  $\{10\bar{1}1\}$  also show maxima in the Wulff plots, with  $\gamma(0001) \approx \gamma(000\bar{1})$  and  $\gamma(\{10\bar{1}1\}) \approx 1.14 \gamma(000\bar{1})$ . For the  $\gamma(\theta)$  plot in Fig. 2(c), there are only 2 minima at the non-polar  $\{11\bar{2}0\}$  and  $\{10\bar{1}0\}$  facets, where  $\gamma(\{10\bar{1}0\}) \approx 0.96 \gamma(\{11\bar{2}0\})$ .

The absolute values of  $\gamma$  for different facets are deduced from the  $\gamma$  ratios of the plots in Fig. 2. As the  $(000\bar{1})$  surface is common to both cross-sectional views of the voids, namely, along  $[1\bar{1}00]$  and  $[1\bar{2}10]$ , this plane is used as a reference to calculate the values of  $\gamma$  for the other planes in Figs. 2(a) and 2(b). DFT calculation uses a slab geometry with a cleavage energy that is twice the surface formation energy.<sup>2</sup> While this is true for non-polar surfaces, separating the slab geometry along c-axis for polar surfaces results in individual Zn and O-terminated surfaces with different surface energies. Therefore, the DFT values for the cleavage energy of the polar surface will not be used. Instead, the surface energy for  $\{11\bar{2}0\} = 1.25 \text{ J/m}^2$  determined by DFT-LDA<sup>2</sup> is first used to estimate  $\gamma$  for the  $(000\bar{1})$  plane from our plot and all other facets in the equilibrium shape. Likewise, for the plan view case in Fig. 2(c), the same  $\gamma$  value for  $\{11\bar{2}0\}$  is also used to find the  $\gamma$  value for  $\{10\bar{1}0\}$ . These  $\gamma$  values are recorded in Table I, with errors within  $\pm 5\%$  over 3 voids at each zone axis. Table I shows that  $\gamma$  acquired in the present work is consistent with the values reported in the literature, particularly non-polar surfaces and  $\{10\bar{1}3\}$ . From Table I,  $\{11\bar{2}7\}$  and  $\{10\bar{1}4\}$  are the most stable planes with the lowest formation energy, followed by  $\{10\bar{1}3\}$ ,  $\{11\bar{2}5\}$ ,  $(000\bar{1})$ ,  $\{10\bar{1}0\}$ , and  $\{11\bar{2}0\}$ .

For the voids analyzed here, the O polar surface is always found to be more prominent than Zn ones. This suggests that O surface is more stable in the presence of H. This corroborates well with previous studies on ZnO polar

surfaces, where He scattering experiments have shown that H-covered O-terminated surface is very stable with  $(1 \times 1)$  reconstruction.<sup>25</sup> On the other hand, prolonged H exposure to the Zn-terminated surface will result in massive reconstruction and disorder.<sup>8,26</sup> It can therefore be concluded that the results in Table I represent the surface formation energy of the facets with H coverage.

Table I shows that the equilibrium shape of ZnO consists of facets with similar formation energy. In particular, the polar  $(000\bar{1})$  O-terminated surface has similar  $\gamma$  value compared to the non-polar planes. This differs from theoretical predictions, where the calculated cleavage energy of polar surfaces is at least  $\sim 2$  times larger than non-polar surfaces.<sup>1,2,4,5</sup> Indeed, the surface formation energy of non-polar planes can be considered as half the cleavage energy, but not for polar surfaces. Moreover, the fact that it is always hard to observe the Zn internal surface suggests that this surface has a very high formation energy. Therefore, the  $\gamma$  summation of the O and Zn terminated surfaces could possibly result in a value larger than the cleavage energy of non-polar surfaces. Furthermore, previous *ab initio* calculations were carried out on clean and unreconstructed surfaces by assuming that stabilization of the polar surfaces is achieved through negative charge transfer from O to Zn terminated surface.<sup>2,4,9</sup> As a high dose of implanted H is used (peak concentration of  $\sim 4 \times 10^{21} \text{ cm}^{-3}$ ), a different surface stabilization mechanism is operating in the samples used in this study. This could be via the adsorption of charged H, which is a possible mechanism to remove charge instability in ZnO polar surfaces.<sup>8,9</sup>

There are two key results in the Wulff construction that warrant further discussions (1) the shorter  $(000\bar{1})$  O polar surface compared to non-polar surfaces (2) the Zn semi-polar surfaces having lower formation energy compared to the O ones when O polar surfaces are more stable compared to the Zn ones. First, a 3D volume within a polar wurtzite semiconductor such as ZnO and the distribution of its facets is limited by its crystallography. In particular, there are only one Zn polar facet and one O polar facet positioned diametrically opposite each other while there is a range of semi-polar planes adjacent to these two facets. With this geometry, wider O polar surface will reduce the inclination of adjacent O semi-polar surfaces and hence make them less polar. Likewise, as there is hardly any Zn polar surface, polarity of the Zn semi-polar surfaces will be maximized. In the present work, polar  $(000\bar{1})$  O-terminated surface shows similar surface energy compared to non- and semi-polar facets, and yet has a much shorter length, which is surprising. They are typically rounded and consequently staggered by some step edges. The complexity of the  $(000\bar{1})$  O-terminated curved surfaces must be such that local minimum extracted from the Wulff plot arises from an agglomeration of complex semi-polar step edges in the vicinity of the  $(000\bar{1})$  surface. Hence, the value extracted from this minimum is doubtfully the real surface energy of  $(000\bar{1})$  surface but a complex average of the  $(000\bar{1})$  and vicinal semipolar surfaces stabilizing this surface.

Second, it is not surprising that O polar surfaces are stable and yet Zn semi-polar surfaces have the lowest surface energy. The polar surfaces and semipolar surfaces are

TABLE I. Surface formation energies (in  $\text{J/m}^2$ ) estimated in this work compared to the literature.

Type	Surface	This work	Previous works
polar	$(000\bar{1})$	1.21	...
non-polar	$\{11\bar{2}0\}$	1.25 (Ref. 2)	1.02, <sup>1</sup> 0.85, <sup>2</sup> 1.25 (Ref. 2)
	$\{10\bar{1}0\}$	1.24, <sup>a</sup> 1.21 <sup>b</sup>	1.01, <sup>1</sup> 0.80, <sup>2</sup> 1.15 (Ref. 2) 0.85, <sup>3</sup> 1.15, <sup>4,5</sup> 2.70 (Ref. 6)
Zn semi-polar	$\{10\bar{1}4\}$	1.09	...
	$\{11\bar{2}7\}$	1.10	...
O semi-polar	$\{10\bar{1}3\}$	1.19	0.99 (Ref. 22)
	$\{11\bar{2}5\}$	1.16	...

<sup>a</sup>XTEM value.

<sup>b</sup>PVTEM value.

different in nature. It has been known that growth rate for ZnO nanowires and thin films is higher along [0001] direction (Zn surface) compared to [000 $\bar{1}$ ] direction (O surface).<sup>27–32</sup> In recent work on ZnO nanowires grown on sapphire, the Zn polar nanowires are found to nucleate at the tip of some pyramid-like structures with O semi-polar surfaces.<sup>29,32</sup> Furthermore, an inversion domain boundary (IDB) is present between the pyramids and the nanowires.<sup>32</sup> These growth results imply that (1) the most stable growth surfaces in these samples are O semi-polar surfaces and Zn polar surfaces and (2) that the extra energy associated with the IDB formation is not a problem. The similarity between the present study and previous growth studies<sup>29,32</sup> suggests that ZnO demonstrates a complex surface energy interplay between its polar, semi-polar, and non-polar surfaces. For ZnO nanowires growth, the O semi-polar and Zn polar surfaces have faster growth rate (which is governed by chemical potential of all the growth precursors). In the present work, the Zn semi-polar surface has the lowest formation energy, and the O polar surface is preferred compared to Zn in H-rich environment. Both results indicate that stable surfaces are a complex aggregation of polar and semi-polar surfaces, not necessarily with the same polarity.

It has also been shown that step energies can be deduced from the discontinuity in  $d\gamma/d\theta$  at the cusp between 2 surfaces in Fig. 2.<sup>13,33</sup> However, Fresnel fringes that are used to image and identify the voids have a finite thickness. With the imaging condition and magnification used in Fig. 1, it is difficult to distinguish any cusps. Therefore, high resolution TEM (HRTEM) analysis was carried out. However, due to low contrast caused by implantation-induced planar defects, only HRTEM images for the voids in PVTEM samples were obtained as shown in Fig. 3. By using step heights  $\alpha(\{11\bar{2}0\}) = 1.62 \text{ \AA}$  and  $\alpha(\{10\bar{1}0\}) = 2.81 \text{ \AA}$ ,<sup>34</sup> and  $\gamma(\{11\bar{2}0\}) = 1.25 \text{ J/m}^2$ ,<sup>2</sup> the resulting step energies are calculated to be  $\beta(\{11\bar{2}0\}) = 4.06 \times 10^{-11} \text{ J/m}$  and  $\beta(\{10\bar{1}0\}) = 3.87 \times 10^{-11} \text{ J/m}$ , for steps along the  $\langle 10\bar{1}0 \rangle$  directions. This results in step energy of 0.066 eV/atom for the  $\{11\bar{2}0\}$  plane and 0.063 eV/atom for the  $\{10\bar{1}0\}$  plane. Note that the error bars in this measurement can be as large as  $\pm 30\%$ .<sup>13</sup>

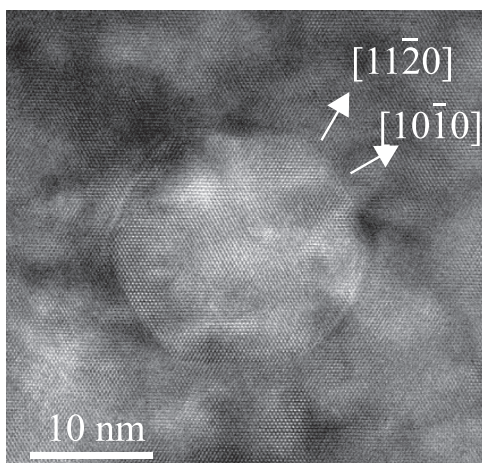


FIG. 3. High resolution TEM plan view image of typical voids along the c-axis.

In conclusion, a reverse Wulff construction is performed on H implantation induced nano-cavities of equilibrium shape in ZnO, to obtain the formation energies of surfaces stabilized with H. O polar surfaces are found to be more stable than Zn polar surfaces. The stable surfaces show similar values in formation energy, with the largest  $\gamma$  ratio  $< 1.25$ . The surface with the lowest formation energy is  $\{10\bar{1}4\}$ , followed by  $\{11\bar{2}7\}$ ,  $\{11\bar{2}5\}$ ,  $\{10\bar{1}3\}$ ,  $\{10\bar{1}0\}$ , and  $\{11\bar{2}0\}$ . The deduced value for the surface formation energy is consistent with reported theoretical values. Surface step energies extracted from the derivative of the surface energy plot are 0.066 eV/atom on  $\{11\bar{2}0\}$  and 0.063 eV/atom on  $\{10\bar{1}0\}$ .

The authors acknowledge financial support from the Australian Research Council and the Norwegian Research Council. Equipment access to the Australian National Fabrication Facilities (ACT node) and the Centre for Advanced Microscopy at the Australian National University is gratefully acknowledged.

<sup>1</sup>Y. J. Hong, J. Yoo, Y.-J. Doh, S. H. Kang, K.-j. Kong, M. Kim, D. R. Lee, K. H. Oh, and G.-C. Yi, *J. Mater. Chem.* **19**, 941 (2009).

<sup>2</sup>B. Meyer and D. Marx, *Phys. Rev. B* **67**, 035403 (2003).

<sup>3</sup>A. Filippetti, V. Fiorentini, G. Cappellini, and A. Bosin, *Phys. Rev. B* **59**, 8026 (1999).

<sup>4</sup>A. Wander, F. Schedin, P. Steadman, A. Norris, R. McGrath, T. S. Turner, G. Thornton, and N. M. Harrison, *Phys. Rev. Lett.* **86**, 3811 (2001).

<sup>5</sup>A. Wander and N. Harrison, *Surf. Sci.* **468**, L851 (2000).

<sup>6</sup>J. E. Jaffe, N. M. Harrison, and A. C. Hess, *Phys. Rev. B* **49**, 11153 (1994).

<sup>7</sup>R. Nosker, P. Mark, and J. Levine, *Surf. Sci.* **19**, 291 (1970).

<sup>8</sup>C. Wöll, *Prog. Surf. Sci.* **82**, 55 (2007).

<sup>9</sup>B. Meyer, *Phys. Rev. B* **69**, 045416 (2004).

<sup>10</sup>R. Wahl, J. V. Lauritsen, F. Besenbacher, and G. Kresse, *Phys. Rev. B* **87**, 085313 (2013).

<sup>11</sup>D. M. Follstaedt, *Appl. Phys. Lett.* **62**, 1116 (1993).

<sup>12</sup>J. Wong-Leung, C. E. Ascheron, M. Petracic, R. G. Elliman, and J. S. Williams, *Appl. Phys. Lett.* **66**, 1231 (1995).

<sup>13</sup>D. J. Eaglesham, A. E. White, L. C. Feldman, N. Moriya, and D. C. Jacobson, *Phys. Rev. Lett.* **70**, 1643 (1993).

<sup>14</sup>S. M. Myers, H. J. Stein, and D. M. Follstaedt, *Phys. Rev. B* **51**, 9742 (1995).

<sup>15</sup>C. H. Seager, S. M. Myers, G. A. Petersen, J. Han, and T. Headley, *J. Appl. Phys.* **85**, 2568 (1999).

<sup>16</sup>S. O. Kucheyev, J. S. Williams, C. Jagadish, J. Zou, C. Evans, A. J. Nelson, and A. V. Hamza, *Phys. Rev. B* **67**, 094115 (2003).

<sup>17</sup>J. Wong-Leung, M. S. Janson, and B. G. Svensson, *J. Appl. Phys.* **93**, 8914 (2003).

<sup>18</sup>K. S. Chan, L. Vines, K. M. Johansen, E. V. Monakhov, J. D. Ye, P. Parkinson, C. Jagadish, B. G. Svensson, and J. Wong-Leung, *J. Appl. Phys.* **114**, 083111 (2013).

<sup>19</sup>D. B. Williams and C. B. Carter, *Transmission Electron Microscopy: A Textbook for Materials Science* (Plenum Press, New York, 1996).

<sup>20</sup>K. S. Chan, C. Ton-That, L. Vines, S. Choi, M. R. Phillips, B. G. Svensson, C. Jagadish, and J. Wong-Leung, *J. Phys. D: Appl. Phys.* **47**, 342001 (2014).

<sup>21</sup>C. Herring, in *Structure and Properties of Solid Surfaces*, edited by R. Gomer and C. S. Smith (University of Chicago Press, Chicago, 1953).

<sup>22</sup>J. Ghatak, J.-H. Huang, P.-C. Huang, Y.-I. Shih, and C.-P. Liu, *J. Electrochem. Soc.* **159**, H239 (2012).

<sup>23</sup>G. Wulff, *Z. Krist.* **34**, 449 (1901).

<sup>24</sup>C. Herring, *Phys. Rev.* **82**, 87 (1951).

<sup>25</sup>M. Kunat, S. G. Girol, T. Becker, U. Burghaus, and C. Wöll, *Phys. Rev. B* **66**, 081402 (2002).

<sup>26</sup>T. Becker, S. Hvel, M. Kunat, C. Boas, U. Burghaus, and C. Wöll, *Surf. Sci.* **486**, L502 (2001).

<sup>27</sup>Z. Wang, T. Tomita, O.-H. Roh, M. Ohsugi, S.-B. Che, Y. Ishitani, and A. Yoshikawa, *Appl. Phys. Lett.* **86**, 011921 (2005).

- <sup>28</sup>Z. L. Wang, X. Y. Kong, and J. M. Zuo, *Phys. Rev. Lett.* **91**, 185502 (2003).
- <sup>29</sup>D. Cherns and Y. Sun, *Appl. Phys. Lett.* **92**, 051909 (2008).
- <sup>30</sup>J. B. Baxter, F. Wu, and E. S. Aydil, *Appl. Phys. Lett.* **83**, 3797 (2003).
- <sup>31</sup>D. A. Scrymgeour, T. L. Sounart, N. C. Simmons, and J. W. P. Hsu, *J. Appl. Phys.* **101**, 014316 (2007).
- <sup>32</sup>G. Perillat-Merceroz, R. Thierry, P.-H. Jouneau, P. Ferret, and G. Feuillet, *Nanotechnology* **23**, 125702 (2012).
- <sup>33</sup>A. Zangwill, *Physics at Surfaces* (Cambridge University Press, New York, 1988), p. 13.
- <sup>34</sup>D. R. Lide, *CRC Handbook of Chemistry and Physics*, 73rd ed. (CRC Press, New York, 1992).